Chemical Science

ROYAL SOCIETY OF CHEMISTRY

EDGE ARTICLE

View Article Online
View Journal | View Issue

Cite this: *Chem. Sci.*, 2022, **13**, 1933

All publication charges for this article have been paid for by the Royal Society of Chemistry

Received 13th October 2021
Accepted 3rd January 2022

DOI: 10.1039/d1sc05647f

rsc.li/chemical-science

Photocytotoxicity and photoinduced phosphine ligand exchange in a Ru(II) polypyridyl complex†

Sean J. Steinke,[a] Sayak Gupta,[b] Eric J. Piechota,[a] Curtis E. Moore,[a] Jeremy J. Kodanko*[b] and Claudia Turro *[a]

Two new tris-heteroleptic Ru(II) complexes with triphenylphosphine (PPh_3) coordination, *cis*-$[Ru(phen)_2(PPh_3)(CH_3CN)]^{2+}$ (**1a**, phen = 1,10-phenanthroline) and *cis*-$[Ru(biq)(phen)(PPh_3)(CH_3CN)]^{2+}$ (**2a**, biq = 2,2′-biquinoline), were synthesized and characterized for photochemotherapeutic applications. Upon absorption of visible light, **1a** exchanges a CH_3CN ligand for a solvent water molecule. Surprisingly, the steady-state irradiation of **2a** followed by electronic absorption and NMR spectroscopies reveals the photosubstitution of the PPh_3 ligand. Phosphine photoinduced ligand exchange with visible light from a Ru(II) polypyridyl complex has not previously been reported, and calculations reveal that it results from a *trans*-type influence in the excited state. Complexes **1a** and **2a** are not toxic against the triple negative breast cancer cell line MDA-MB-231 in the dark, but upon irradiation with blue light, the activity of both complexes increases by factors of >4.2 and 5.8, respectively. Experiments with PPh_3 alone show that the phototoxicity observed for **2a** does not arise from the released phosphine ligand, indicating the role of the photochemically generated ruthenium aqua complex on the biological activity. These complexes represent a new design motif for the selective release of PPh_3 and CH_3CN for use in photochemotherapy.

Introduction

Ruthenium(II) polypyridyl complexes exhibit useful excited state properties that have been explored in photochemotherapy (PCT), photodynamic therapy (PDT), and solar energy conversion, among other applications.[1–8] The spatiotemporal control possible with these complexes shows promise in alternative cancer therapies, circumventing systemic toxicity present in traditional cancer therapies, such as approved platinum drugs.[9] Typically, PCT and PDT agents are activated by the absorption of visible light in the irradiated area, leading to the population of excited states that can produce cytotoxic $^1O_2$ for PDT or induce the release of a therapeutic agent in PCT. Unlike complexes used in photochemotherapy, PDT agents rely on the presence of oxygen, which can represent a drawback in the hypoxic environments found in solid tumors,[10–12] making PCT agents an important area of research to advance photoinduced treatments.[13–15]

Coordination to the Ru(II) center through a Lewis basic site, such as a nitrile or pyridine functional group, have been explored as PCT agents and for dual PCT/PDT activity, since many drugs that can be photoreleased possess one of these groups able to coordinate to a transition metal center.[16–20] A frequent challenge, however, is the ability of other strong field ligands, such as phosphines, to undergo photoinduced dissociation. Importantly, molecules with a triphenylphosphinium group and cationic compounds with a triphenylphosphine (PPh_3) ligand have been shown to enhance cellular uptake,[21,22] leading to an interest in the investigation of divalent ruthenium triphenylphosphine complexes for PCT.

Phosphine ligands, such as PMe_3 (Me = methyl) and PPh_3, have been shown to act as ancillary ligands that increase or promote the photosubstitution of other monodentate ligands in the Ru(II) coordination sphere.[23–25] In particular, PR_3 (R = Me, Ph) ligands are generally stronger field ligands relative to N–coordinated pyridine and acetonitrile. Strong π-backbonding to phosphine ligands has also been used to modify the electronic structure on the ruthenium center to reduce the overpotential of CO_2 reduction catalysts and to tune the absorption and emission properties.[26–29] Whereas CH_3CN and pyridine have been previously shown to undergo photoinduced ligand exchange in Ru(II) complexes, phosphine ligands are largely inert to photosubstitution.[4,24,29–34] The design of complexes that can selectively photodissociate phosphines can enable the use of drugs with phosphine motifs in PCT,[35–37] as well as the synthesis of supported catalysts patterned with selective irradiation.[38–40]

[a]*Department of Chemistry and Biochemistry, The Ohio State University, Columbus, OH, 43210, United States. E-mail: turro.1@osu.edu*

[b]*Department of Chemistry, Wayne State University, Detroit, MI, 48208, United States. E-mail: jkodanko@wayne.edu*

† Electronic supplementary information (ESI) available: ^1H and $^{31}P\{H\}$ NMR spectra, electrochemical and X-ray crystallographic data, and DFT information (PDF). CCDC 2108338, 2109146, 2108340 and 2108925. For ESI and crystallographic data in CIF or other electronic format see DOI: 10.1039/d1sc05647f

In the present work, two new heteroleptic Ru(II) complexes containing one PPh_3 and one CH_3CN ligand, *cis*-$[Ru(phen)_2(PPh_3)(CH_3CN)]^{2+}$ (**1a**, phen = 1,10-phenanthroline) and *cis*-$[Ru(biq)(phen)(PPh_3)(CH_3CN)]^{2+}$ (**2a**, biq = 2,2′-biquinoline), were synthesized and characterized, and their structures are shown in Fig. 1. The electronic absorption, electrochemistry, and photochemistry of **1a** and **2a** were investigated and compared to those of their bis-acetonitrile analogs, *cis*-$[Ru(phen)_2(CH_3CN)_2]^{2+}$ (**1b**) and *cis*-$[Ru(biq)(phen)(CH_3CN)_2]^{2+}$ (**2b**). Based on the steric distortion introduced by the bulky PPh_3 ligand, complexes **1a** and **2a** were expected to exhibit more facile CH_3CN dissociation. While **1a** exhibits photoinduced CH_3CN exchange upon visible light excitation, **2a** represents the first example of photoinduced exchange of a PPh_3 ligand from a Ru(II) polypyridyl complex, a surprising departure from the commonly observed substitutional inertness of PPh_3 ligands. Single-crystal X-ray structures of **1a**, **2a**, and the photoproduct of **2a** following photolysis in CH_3CN and pyridine (**I**), were collected and calculations were performed on **1a** and **2a** to gain better understanding of the origin of the unusual photoreactivity. In addition, complexes **1a** and **2a** were evaluated for their toxicity against the triple-negative breast cancer MDA-MB-231 cell line in the dark and upon irradiation. The present findings show enhanced activity following photoinduced ligand dissociation for both complexes and that PPh_3 release from **2a** results in a modest increase in toxicity as compared to CH_3CN photodissociation in **1a**. Importantly, both **1a** and **2a** exhibit significantly greater photoactivity than related complexes without PPh_3 in their coordination sphere. The present work is consistent with greater cellular uptake by the PPh_3-containing complexes, laying the groundwork for the design of new photoactive complexes with enhanced activity.

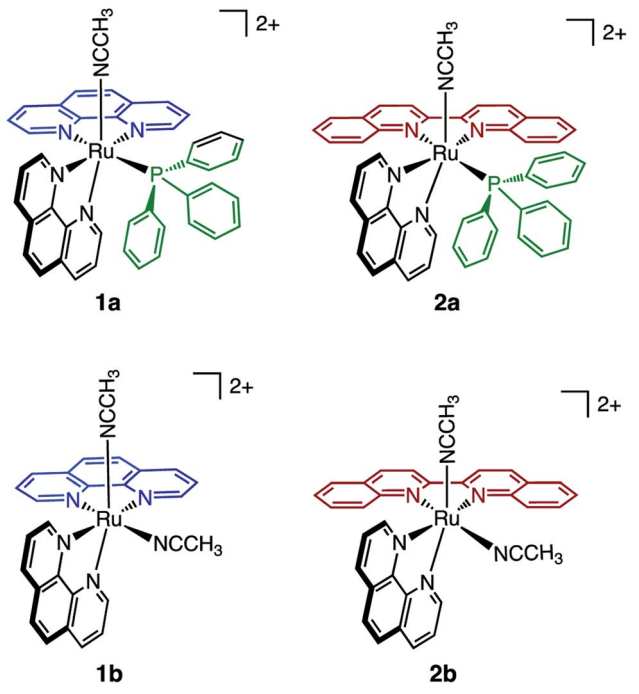

Fig. 1 Schematic representation of the molecular structures of **1a**, **1b**, **2a**, and **2b**.

Experimental

Materials

All materials were used as received without further purification, including 1,10-phenanthroline, 2,2′-biquinoline, CD_3CN, CD_3OD, $(CD_3)_2CO$, lithium chloride, pyridine, silver tetrafluoroborate, tetrabutylammonium hexafluorophosphate, and triphenylphosphine which were purchased from Sigma-Aldrich. Ethanol (200 proof) was obtained from Decon Laboratories, acetone, acetonitrile, dichloromethane, diethyl ether, *N*,*N*-dimethylformamide, 85% H_3PO_4, and toluene were acquired from Fischer Scientific, and ammonium hexafluorophosphate was purchased from Oakwood Chemical. Complexes **1b** and **2b**,[41] $[Ru(phen)_2Cl_2]$,[42] $[Ru(p\text{-cymene})Cl_2]_2$,[43] and triphenylphosphine oxide[44] were prepared according to literature procedures.

$[Ru(phen)_2(PPh_3)(Cl)](PF_6)$

$[Ru(phen)_2Cl_2]$ (0.16 g, 0.30 mmol), triphenylphosphine (0.14 g, 0.53 mmol), and excess LiCl were added to 10 mL ethanol/water (1 : 1, v/v) mixture sparged for 15 min with N_2. The reaction mixture was refluxed for 4 h under a nitrogen atmosphere, allowed to cool, concentrated by rotary evaporation, and then precipitated by adding it dropwise to a concentrated NH_4PF_6 solution. The product was purified by column chromatography, using a deactivated neutral alumina stationary phase and a 1 : 2 toluene : acetone mobile phase. The solvent was removed from the fraction containing the product *via* rotary evaporation, producing a dark orange solid (0.078 g, 29% yield). ^{1}H NMR (400 MHz, $(CD_3)_2CO$, Fig. S1†): δ 9.72 (d, 1H, J = 5.4 Hz), 8.77 (m, 2H), 8.68 (d, 1H, J = 8.2 Hz), 8.55 (dd, 1H, J = 5.7, 3.9 Hz), 8.37 (s, 2H), 8.36 (d, 1H, J = 1.3 Hz), 8.30 (d, 1H, J = 8.8), 8.23 (dd, 1H, J = 20.3, 9.0 Hz), 8.13 (d, 1H, J = 8.8 Hz), 7.90 (dd, 1H, J = 8.2, 5.3 Hz), 7.86 (dd, 1H, J = 8.2, 5.3 Hz), 7.77 (dd, 2H, J = 8.3, 5.3 Hz), 7.65 (d, 1H, 5.3 Hz), 7.53 (m, 2H), 7.37 (t, 5H, J = 8.7 Hz), 7.27 (t, 2H, J = 7.6 Hz), 7.11 (m, 6H). ^{31}P{H} NMR (400 MHz, $(CD_3)_2CO$, Fig. S2†): δ 45.1 (s, 1P).

$[Ru(phen)_2(PPh_3)(CH_3CN)](PF_6)_2$ (1a)

$[Ru(phen)_2(PPh_3)Cl](PF_6)$ (0.058 g, 0.064 mmol) was dissolved in 10 mL of acetonitrile/H_2O (1 : 1, v/v) mixture and, under an atmosphere of nitrogen, was refluxed overnight. After cooling to room temperature, the reaction solution was added dropwise to a concentrated aqueous NH_4PF_6 solution. The precipitate that formed was collected by filtering over Celite and purified on a neutral alumina column eluted with a 1 : 2 toluene : acetone mobile phase. The purified solution was collected and the solvent was removed *via* rotary evaporation, affording the desired product as a yellow-orange solid (0.031 g, 53% yield). ^{1}H NMR (400 MHz, CD_3CN, Fig. S3†): δ 9.41 (d, 1H, J = 5.3 Hz), 9.09 (d, 1H, J = 5.2 Hz), 8.82 (dd, 1H, J = 8.4, 1.2 Hz), 8.59 (dd, 1H, J = 8.3, 1.2 Hz), 8.55 (dd, 1H, J = 8.2, 1.3 Hz), 8.37 (dd, 1H, J = 8.3, 1.2 Hz), 8.24 (dd, 2H, J = 28, 8.8 Hz), 8.13 (dd, 2H, J = 18, 8.8 Hz), 7.90 (dd, 1H, J = 3.0, 5.3 Hz), 7.75 (dd, 1H, J = 3.0, 5.3 Hz), 7.49 (m, 1H), 7.43 (m, 1H), 7.37 (m, 4H), 7.19 (m, 7H), 7.03 (td, 6H, J = 9.4, 1.1 Hz), 2.17 (s, 3H). ^{31}P{H} NMR (400 MHz, CD_3CN,

Fig. S4†): δ 45.3 (s, 1P). ESI-MS(+): $[M–PF_6]^+$ m/z = 910.193 (calc. m/z = 910.123).

[Ru(*p*-cymene)(phen)Cl]

$[Ru(p\text{-cymene})Cl_2]_2$ (0.30 g, 0.50 mmol) and 1,10-phenanthroline (0.19 g, 1.1 mmol) were dissolved in 4 mL acetonitrile and refluxed under a nitrogen atmosphere for 2 h, during which time a change from a red to orange solution was observed. A yellow-orange solid was collected by filtering over Celite (0.37 g, 82% yield). ^{1}H NMR (400 MHz, CD_3OD, Fig. S5†): δ 9.84 (d, 2H, J = 5.5 Hz), 8.84 (d, 2H, J = 8.3 Hz), 8.21 (s, 2H), 8.11 (dd, 2H, J = 8.3, 5.3 Hz), 6.23 (d, 2H, J = 6.5 Hz), 6.00 (d, 2H, J = 6.2 Hz), 2.66 (q, 1H, J = 7.0 Hz), 2.27 (s, 3H), 0.99 (d, 6H, J = 6.9 Hz).

[Ru(biq)(phen)Cl_2]

[Ru(*p*-cymene)(phen)Cl] (0.33 g, 0.68 mmol), 2,2′-biquinoline (0.18 g, 0.69 mmol), and excess LiCl were dissolved in 2 mL *N*,*N*-dimethylformamide and refluxed under a nitrogen atmosphere for 90 min. After refluxing was complete, the reaction mixture was allowed to cool to room temperature and then added dropwise to 30 mL aqueous LiCl solution, producing a dark green solution. A dark green solid was collected *via* vacuum filtration and was rinsed three times each with 20 mL H_2O and 20 mL diethyl ether. The solid was dissolved using 1 L of a CH_2Cl_2/methanol (1 : 1, v/v) solvent mixture, which was then removed by rotary evaporation to afford the desired product as a dark green solid (0.18 g, 44% yield).

[Ru(biq)(phen)(PPh_3)Cl](PF_6)

[Ru(biq)(phen)Cl_2] (0.048 g, 0.080 mmol), triphenylphosphine (0.039 g, 0.15 mmol), and excess LiCl were added to a 10 mL ethanol/water (1 : 1, v/v) mixture sparged for 15 min with N_2. The reaction mixture was refluxed for 4 h under a nitrogen atmosphere, allowed to cool, concentrated by rotary evaporation, and then added dropwise to a concentrated NH_4PF_6 solution to produce a purple precipitate. The product was purified by column chromatography, using a neutral alumina stationary phase and an acetone mobile phase. The solvent was removed from the fraction containing the product *via* rotary evaporation producing a red-purple solid (0.052 g, 66% yield). ^{1}H NMR (400 MHz, $(CD_3)_2CO$, Fig. S6†): δ 10.21 (s, 1H), 8.90 (m, 4H), 8.61 (d, 2H, J = 7.8 Hz), 8.53 (d, 1H, J = 8.1 Hz), 8.30 (t, 2H, J = 7.3 Hz), 8.12 (d, 1H, J = 8.2 Hz), 8.06 (dd, 1H, J = 8.1, 5.5 Hz), 7.85 (dd, 3H, J = 32.8, 9.0 Hz), 7.63 (m, 3H), 7.52 (t, 1H, J = 7.6 Hz), 7.28 (t, 2H, 7.5 Hz), 7.17 (s, 3H), 6.95 (m, 12H). ^{31}P{H} NMR (400 MHz, $(CD_3)_2CO$, Fig. S7†): δ 42.5 (s, 1P).

[Ru(biq)(phen)(PPh_3)(CH_3CN)](PF_6)$_2$ (2a)

[Ru(biq)(phen)(PPh_3)Cl](PF_6) (0.044 g, 0.038 mmol) and $AgBF_4$ (0.019 g, 0.099 mmol) were dissolved in 10 mL of a CH_3CN/H_2O (1 : 1, v/v) mixture and were refluxed overnight under a N_2 atmosphere. After cooling to room temperature, the reaction mixture was added dropwise to a concentrated NH_4PF_6 solution, precipitate was collected by filtering over Celite, and then purified *via* bulk recrystallization using vapor diffusion of ether into a concentrated solution of **2a** in acetonitrile, which afforded a red-orange solid (0.013 g, 35% yield). ^{1}H NMR (400 MHz, CD_3CN, Fig. S8†): δ 10.1 (d, 1H, J = 5.3 Hz), 8.96 (d, 2H, J = 8.7 Hz), 8.69 (d, 2H, J = 8.8 Hz), 8.30 (m, 5H), 8.19 (m, 5H), 8.07 (dd, 2H, J = 5.4, 2.8 Hz), 7.64 (m, 4H), 7.54 (m, 5H), 7.28 (td, 3H, J = 7.4, 1.1 Hz), 7.21 (td, 3H, J = 7.8, 1.5 Hz), 7.16 (td, 3H, J = 7.9, 1.4 Hz), 2.34 (s, 3H). ^{31}P{H} NMR (400 MHz, CD_3CN, Fig. S9†): δ 42.3 (s, 1P). ESI-MS(+): $[M–PF_6]^+$ m/z = 986.252 (calc. m/z = 986.155).

Instrumentation and methods

Electronic absorption spectra were collected using a Hewlett-Packard 8454 diode array spectrophotometer in 1 cm × 1 cm quartz cuvettes. The irradiation source for photolysis experiments was a 150 W Xe arc lamp (UHSIO) in a MilliArc lamp housing unit equipped with an LPS-220 power supply and an LPS-221 igniter (PTI). Irradiation wavelengths for quantum yield determination were selected by using bandpass and long-pass filters (CVI Melles Griot). Samples for photolysis were prepared under red light, sealed in an NMR tube (NMR) or cuvette (UV-Vis), and purged with N_2 for 15 min prior to irradiation.

The ^{1}H and ^{31}P{H} NMR spectra were obtained using a Bruker 400 MHz DPX instrument in CD_3CN, $(CD_3)_2CO$, or CD_3OD. ^{1}H chemical shifts were referenced to the residual protonated solvent peak and ^{31}P{H} shifts were referenced to an external 85% H_3PO_4 standard (0 ppm). ^{1}H and ^{31}P{H} NMR photolysis experiments were performed in CD_3CN. Electrospray ionization mass spectrometry (ESI-MS) was performed using a Bruker microTOF instrument. For ESI-MS experiments, samples were dissolved in CH_3CN and referenced to a sodium trifluoroacetate standard.

Electrochemistry experiments were performed on a BASi model CV-50 W voltammetric analyzer (Bioanalytical Systems, Inc.) with a three-electrode cell utilizing a glassy carbon working electrode, a Pt wire auxiliary electrode, and a saturated Ag/AgCl (3 M NaCl) reference electrode. Samples were dissolved in acetonitrile containing 0.1 M tetrabutylammonium hexafluorophosphate ($TBAPF_6$) as an electrolyte, data was collected at a scan rate of 200 mV s^{-1}, and ferrocene was added at the end of each experiment as an internal reference (+0.43 V *vs.* Ag/AgCl in acetonitrile).[45]

Crystals suitable for X-ray diffraction were obtained through vapor diffusion of diethyl ether into concentrated acetonitrile or pyridine solutions of the desired complex. Single crystal X-ray diffraction for **2a** was performed using a dark red rectangular plate crystal in a nitrogen gas stream at 150 K. The diffraction pattern was collected using a Nonius Kappa APEXII CCD diffractometer and Mo K_α radiation (λ = 0.7107 Å). Data were integrated using the Bruker SAINT software program and scaled using the SADABS software program. Structures were solved and refined with the Bruker SHELXT Software Package within APEX2 and Olex2. Other single crystal X-ray diffraction measurements were performed on a Bruker Kappa Photon II CPAD diffractometer equipped with Mo K_α radiation (**1a** and **2b**, λ = 0.71073 Å) or Cu K_α radiation (**I**, λ = 1.54178 Å) using a dark red crystal (**1a**), orange plate (**2b**), or red blade (**I**) in a nitrogen gas stream

at 100(2) K. The data were integrated using the Bruker SAINT software program and scaled using the SADABS software program. Solution by direct methods (SHELXT) produced a complete phasing model consistent with the proposed structure.

Spin restricted and unrestricted density functional theory (DFT) calculations were performed using the Gaussian09 program package.[46] Geometry optimizations and vibrational frequency calculations were performed with the SDD[47] basis set on Ru and the TZVP[48] basis set on all other atoms with the PBE exchange–correlation functional.[49,50] The geometries of **1a**, **2a**, and **2b** were fully optimized starting from X-ray crystal structures and were verified to have positive harmonic frequencies, confirming the calculated structures as electronic energy minima. Molecular orbital calculations utilized the hybrid functional B3LYP,[51–53] with the SDD basis set on Ru and the TZVP basis set on all other atoms. Spin densities were calculated using Mulliken population analysis (MPA) methods. Molecular orbitals from the Gaussian calculations were plotted using the Chemcraft program,[54] and the analysis of the molecular orbitals and Mayer bond order calculations were performed using AOMix-FO within the AOMix program.[55,56]

The cell viability of all the synthesized complexes were determined by plating MDA-MB-231 cells in a 96 well plate at a density of 7000 cells per well in Dulbecco's Modified Eagle's Medium (DMEM) supplemented with 10% FBS and 1000 units per mL penicillin/streptomycin. The plates were incubated overnight in a 37 °C humidified incubator ventilated with 5% CO_2. The media was aspirated off and then quadruplicate wells were treated with DMEM supplemented with 10% FBS and 1000 units per mL penicillin/streptomycin containing different concentrations (30 μM to 500 nM) of the synthesized complexes in 1% DMSO. Plates containing wells with no cells were designated as blank wells whereas wells with cells that were not treated with the compound but only DMEM supplemented with 10% FBS and 1000 units per mL penicillin/streptomycin containing 1% DMSO (vehicle) were designated as control wells. The plates were then again incubated in a 37 °C humidified incubator ventilated with 5% CO_2. After 1 h of incubation, the cells were either irradiated with blue light (t_{irr} = 20 min, λ_{irr} = 460–470 nm, 56 J cm^{-2}) or kept in the dark. After 20 minutes, the plates were placed in a 37 °C humidified incubator with 5% CO_2 for 72 h, after which time, 10 μL of 3-(4,5-dimethylthiazol-2-yl)diphenyl tetrazolium bromide (MTT) reagent (5 mg mL^{-1} in PBS) was added to each well of the 96 well plate and incubated in a 37 °C humidified incubator ventilated with 5% CO_2 for 2 h. The media was then aspirated off and 100 μL of DMSO was added. The plates were then shaken for 20 min to ensure complete dissolution of the purple formazan crystals formed. Absorbance of each well was then measured at 570 nm. The mean absorbance values of the blank wells were calculated and subtracted from absorbance values for each well treated with a certain concentration of a compound. The absorbance of the control wells was also taken and subtracted with the average of the blank wells. The mean of these corrected control absorbances were then calculated. Viability of the cells was finally determined by dividing the corrected absorbance of the compound wells by the mean corrected absorbance of the control wells and expressing the mean of the ratio as a percentage value. The % viability was plotted against the log of concentration (in molarity) of the compounds and the antilog of the concentration value at 50% viability was used to determine the EC_{50} value of each complex against MDA-MB-231 cells.

Results and discussion

Electronic absorption and electrochemistry

The electronic absorption spectra of **1a**, **1b**, **2a**, and **2b** are shown in Fig. 2 and the corresponding absorption maxima and extinction coefficients are listed in Table 1. The singlet metal-to-ligand charge transfer (^{1}MLCT) absorption maxima of **1a** in CH_3CN, attributed to Ru(dπ)→phen(π*) transitions, are observed at 372 nm and 411 nm. For **2a** the Ru(dπ)→phen(π*) and Ru(πp)→biq(π*) ^{1}MLCT bands are observed at 407 nm and 477 nm, respectively, in CH_3CN. The substitution of one of the phen ligands in **1a** for biq in **2a** results in a bathochromic shift in the ^{1}MLCT absorption maximum, as expected from the increased conjugation and subsequently increased π-accepting character of the biq ligand as compared to phen. A similar shift is observed in the ^{1}MLCT maxima of the bis-acetonitrile analogs, **1b** and **2b**, at 420 nm and 497 nm, respectively. In addition, the lower energy of the ^{1}MLCT transitions in **1b** and **2b**, as compared to the corresponding peaks in **1a** and **2a**, are consistent with the increased π-accepting character of the phosphine ligand as compared to acetonitrile.[26,31,57–59]

The electrochemical reduction potentials for complexes **1a** and **2a** obtained from cyclic voltammetry (CV) experiments are listed in Table 1 and the corresponding CVs are shown in Fig. S10,† and are compared to those previously reported for **1b** and **2b**.[41] The first reversible reduction events of **1a** and **1b** are localized on one of the phen ligands, with $E_{1/2}$ values at −1.29 V and −1.34 V *vs.* Ag/AgCl, respectively, and compare well to those reported for related complexes.[60,61] In contrast, the first reduction couples of **2a** and **2b** observed at −0.82 V and −0.86 V *vs.* Ag/AgCl, respectively, are centered on the biquinoline ligand in each complex, consistent with the lower energy lowest unoccupied π* orbital in biq and similar to those measured in related complexes.[60,62]

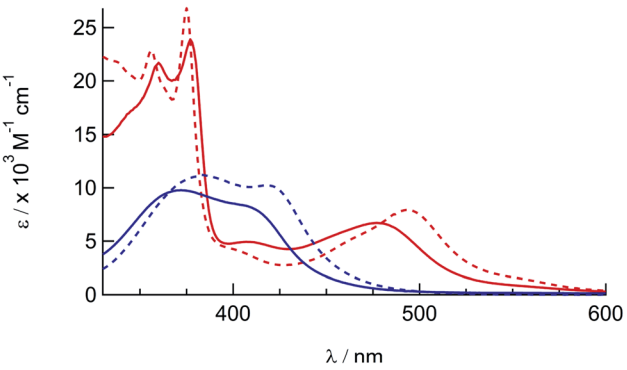

Fig. 2 Electronic absorption spectra of **1a** (solid blue), **1b** (dashed blue), **2a** (solid red), and **2b** (dashed red) in CH_3CN.

Table 1 Electronic absorption maxima (λ_{abs}), molar absorption coefficients (ε), and electrochemical half-wave reduction potentials ($E_{1/2}$) in CH_3CN

Complex	λ_{abs}/nm ($\varepsilon/\times 10^3$ M^{-1} cm^{-1})	$E_{1/2}$/V[a]
1a	372 (9.1), 411 (7.4)	+1.62, −1.29, −1.51
1b[b]	383 (11.2), 420 (10.2)	+1.50, −1.34, −1.50
2a	360 (18), 377 (20), 407 (4.2), 477 (5.7)	+1.67, −0.82, −1.36[c]
2b[b]	356 (23), 375 (27), 406 (3.9), 497 (7.8)	+1.55, −0.86, −1.40

[a] 0.1 M $TBAPF_6$, *vs.* Ag/AgCl in CH_3CN. [b] From ref. 41. [c] Irreversible.

The second reduction wave is localized on the phen ligand in **2a** and **2b**, observed at −1.36 V and −1.40 V *vs.* Ag/AgCl, respectively, and on the remaining phen ligand in **1a** and **1b**, at −1.51 V and −1.50 V *vs.* Ag/AgCl, respectively. The reversible oxidation events ranging from +1.50 to +1.67 V *vs.* Ag/AgCl are assigned to the $Ru^{III/II}$ redox couple (Fig. S10† and Table 1). The ~120 mV shift of the $Ru^{III/II}$ couples to more positive potentials in **1a** and **2a** relative to those in **1b** and **2b**, respectively, is consistent with the greater π-accepting character of triphenylphosphine, stabilizing the highest occupied molecular orbital (HOMO). Taken together, the electrochemical data indicate that the synthetic substitution of PPh_3 in **1a** and **2a** for CH_3CN in **1b** and **2b** primarily affects the energy of the Ru(dπ) t_{2g}-type orbitals.

Photochemistry

In order to explore the light-induced ligand dissociation in complexes **1a** and **2a**, their photoreactivity was investigated by monitoring changes in the electronic absorption and ^1H and $^{31}P\{H\}$ NMR spectra as a function of irradiation time. Irradiation of **1a** in water (<5% acetone) with visible light results in a decrease in intensity of the absorption peak at 372 nm and a concomitant increase in the 430–550 nm range with a shoulder at 455 nm, along with an isosbestic point at 407 nm (Fig. 3a). The presence of the isosbestic point is indicative of the reaction proceeding from the starting material to a single product. The changes to the ^1H NMR spectrum of **1a** in CD_3CN were also monitored as a function of irradiation time, resulting in a decrease in the resonance at 2.17 ppm associated with CH_3CN bound to ruthenium and the concomitant appearance of a resonance at 1.96 ppm, corresponding to free CH_3CN (Fig. 3b). These data indicate that the irradiation of **1a** results in the substitution of the CH_3CN ligand with a solvent molecule, in this case CD_3CN, with the absence of any additional photochemical reactions. The bathochromic shift in Fig. 3a is also consistent with this conclusion, as the photolysis of **1a** in water results in the formation of *cis*-$[Ru(phen)_2(PPh_3)(H_2O)]^{2+}$, where the bound CH_3CN is substituted for the weaker-field, π-donating H_2O ligand, thus raising the energy of the Ru(dp) t_{2g}-type set and lowering the energy of the ^{1}MLCT transition.[34,63,64]

The irradiation of **2a** in CH_3CN results in a decrease in the absorption at 407 nm and an increase a peak at 497 nm, with two isosbestic points at 396 nm and 478 nm (Fig. 4a). As shown in Fig. 4b, the spectrum of the photoproduct is nearly identical to that of **2b**, providing evidence that the irradiation of **2a**

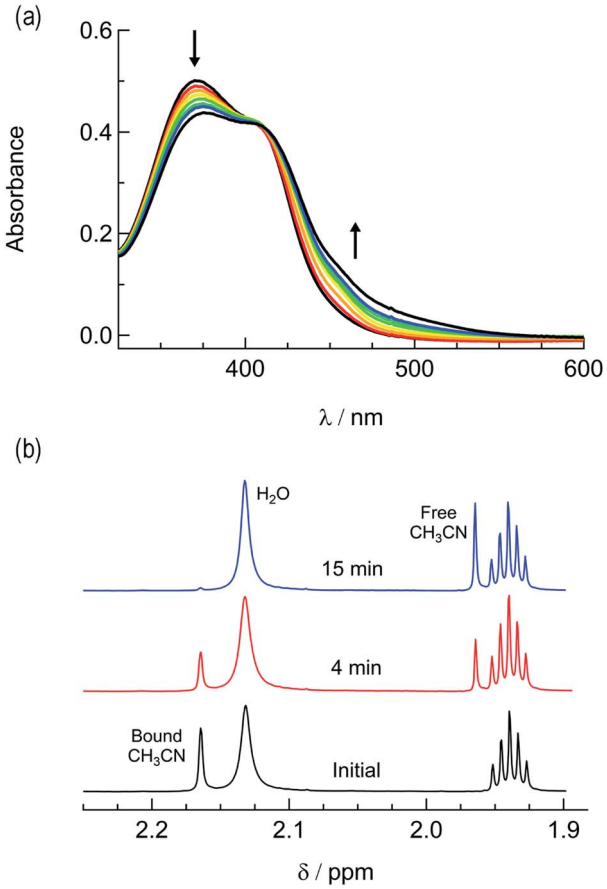

Fig. 3 Changes following the irradiation of **1a** ($\lambda_{irr} \geq 395$ nm) to the (a) electronic absorption spectrum in H_2O, t_{irr} = 0–30 min, and (b) ^1H NMR spectrum in CD_3CN, t_{irr} = 0, 4, and 14 min.

results in the photoinduced dissociation of the PPh_3 ligand generating *cis*-$[Ru(biq)(phen)(CH_3CN)_2]^{2+}$, compound **2b**. The changes in the ^1H NMR spectra of **2a** in CD_3CN recorded as a function of irradiation time are also consistent with the exchange of the phosphine ligand following visible light irradiation (Fig. 5a). For example, the resonance at 2.34 ppm, associated with the ruthenium-bound CH_3CN ligand, decreases in intensity upon irradiation, with the concomitant growth of a peak at 2.47 ppm, associated with the photoproduct *cis*-$[Ru(biq)(phen)(CH_3CN)(CD_3CN)]^{2+}$, similar to the resonances observed for the coordinated CH_3CN ligands in **2b**.[41]

The changes to the $^{31}P\{H\}$ NMR spectra of **2a** upon irradiation provide additional evidence for PPh_3 exchange, where a decrease in intensity of the $^{31}P\{H\}$ resonance at 42.3 ppm, associated with coordinated PPh_3 is observed during the photolysis (Fig. 5b). Concurrently, a $^{31}P\{H\}$ resonance corresponding to triphenylphosphine oxide centered at 26.0 ppm appeared as a function of irradiation time (Fig. 4d and S11†). Importantly, following 15 minutes of irradiation of **2a**, the $^{31}P\{H\}$ resonance associated with bound PPh_3 completely disappears, while the ^1H peaks of the photoproduct *cis*-$[Ru(biq)(phen)(CH_3CN)(CD_3CN)]^{2+}$ persisted. In addition, the resonance at 1.96 ppm associated with free CH_3CN appears

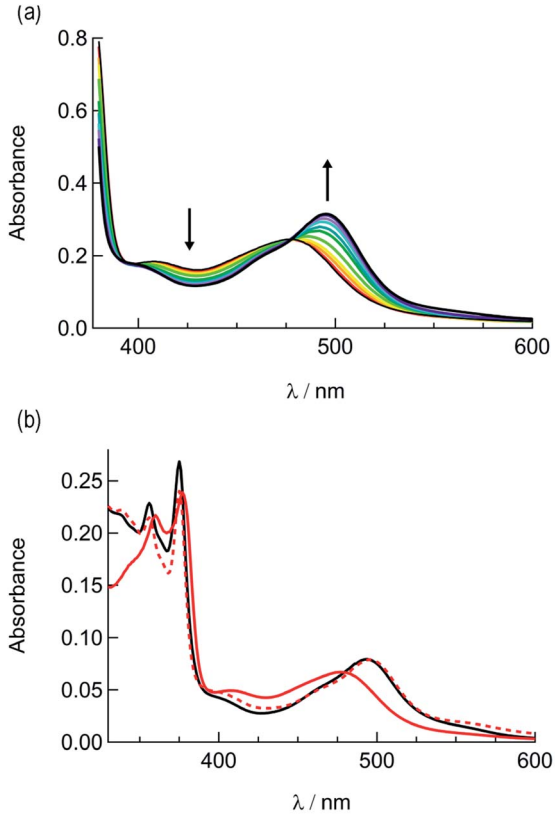

Fig. 4 (a) Changes in the electronic absorption spectrum of **2a** in CH_3CN following irradiation, t_{irr} = 0–5 min and (b) electronic absorption spectra of **2a** before irradiation (solid red), following 30 min irradiation (dashed red), and **2b** (black).

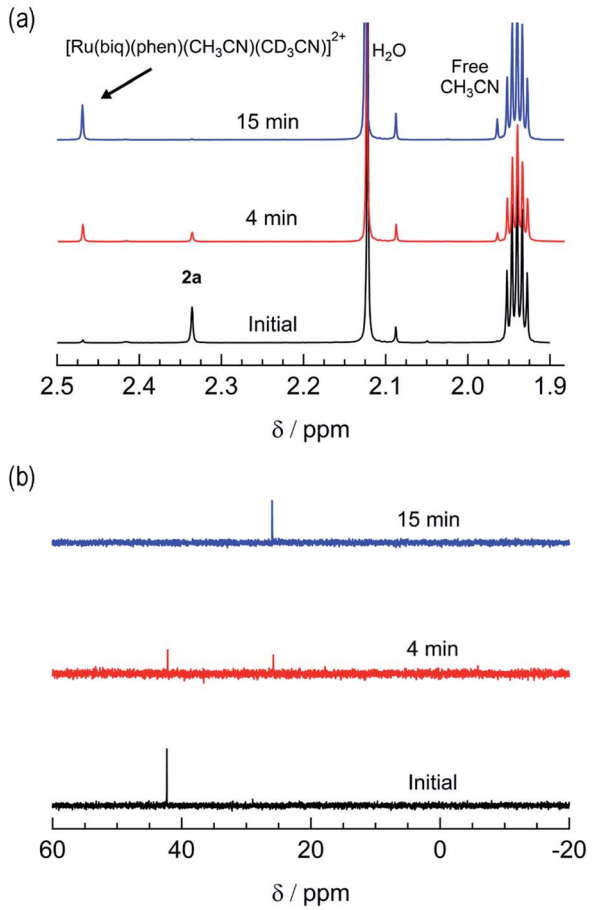

Fig. 5 Changes in the (a) ^{1}H and (b) ^{31}P{H} NMR spectra of **2a** in CD_3CN at t_{irr} = 0, 4, and 15 min ($\lambda_{irr} \geq 395$ nm).

concomitantly with the peak at 2.47 ppm, indicating CH_3CN is also photodissociated albeit not completely on the timescale of the NMR photolysis experiment.

Based on these results, the question remains whether the irradiation of **2a** results in dissociation of both PPh_3 and CH_3CN from the starting material, or if CH_3CN exchanges only from the intermediate photoproduct *cis*-$[Ru(biq)(phen)(CH_3CN)(CD_3CN)]^{2+}$ after the initial dissociation of PPh_3 from the starting complex. In an effort to address this point and trap the product of the first ligand exchange step, photolysis experiments were performed in the coordinating solvent pyridine under identical illumination conditions to those previously discussed in acetonitrile, and the results are shown in Fig. 6. Inspection of Fig. 6a reveals one set of isosbestic points at early irradiation times, up to ~2.5 min, observed at 316 nm, 448 nm, and 500 nm, and the decrease of the peak associated with **2a** at 490 nm with the appearance of a band at 540 nm. A second set of isosbestic points is evident at later times (Fig. 6b), from ~3.5 min to 20 min, at 338 nm, 361 nm, and 550 nm, with a loss of the species with absorption at 540 nm and the formation of the final product with maximum at 590 nm. These results point at the formation of solely one initial intermediate, **I**, with maximum at 540 nm, which then goes on to exchange a second ligand to generate the final product with a peak at 590 nm, assigned to *cis*-$[Ru(biq)(phen)(py)_2]^{2+}$ (**3**). As expected from the ability of CH_3CN to π-backbond with the Ru(dπ) t_{2g}-type orbitals that is not present in pyridine, the ^{1}MLCT maximum of *cis*-$[Ru(biq)(phen)(py)_2]^{2+}$, **3**, is red-shifted compared to that of the product **2b**, *cis*-$[Ru(biq)(phen)(CH_3CN)_2]^{2+}$, in Fig. 4a.

The intermediate **I** was identified as *cis*-$[Ru(biq)(phen)(py)(CH_3CN)]^{2+}$, generated by absorption of a single photon by **2a** and photosubstitution of the triphenylphosphine ligand for a solvent pyridine molecule. Identification was supported, in conjunction with ^{31}P{H} NMR spectra (Fig. 5b), by obtaining a single-crystal X-ray diffraction structure of the photoproduct generated by irradiating a solution of **2a** in pyridine with ≥ 395 nm light for 90 s (Fig. S12 and Table S1†). No further spectral changes took place after the conclusion of irradiation, indicating **I** is stable in the dark. This conclusion further supported by the persistence of the complex in a pyridine solution as the compound recrystallized *via* diethyl ether diffusion.

The presence of the two sets of isosbestic points permits determination of time-dependent concentrations of the three individual species in solution: **2a**, **I**, and **3**, during the photolysis, where **I** represents an intermediate species. The deconvolution of the associated spectra is possible from the known absorption spectra and molar extinction coefficients of **2a** and **3**, and the details of the analysis are presented in the ESI, Table

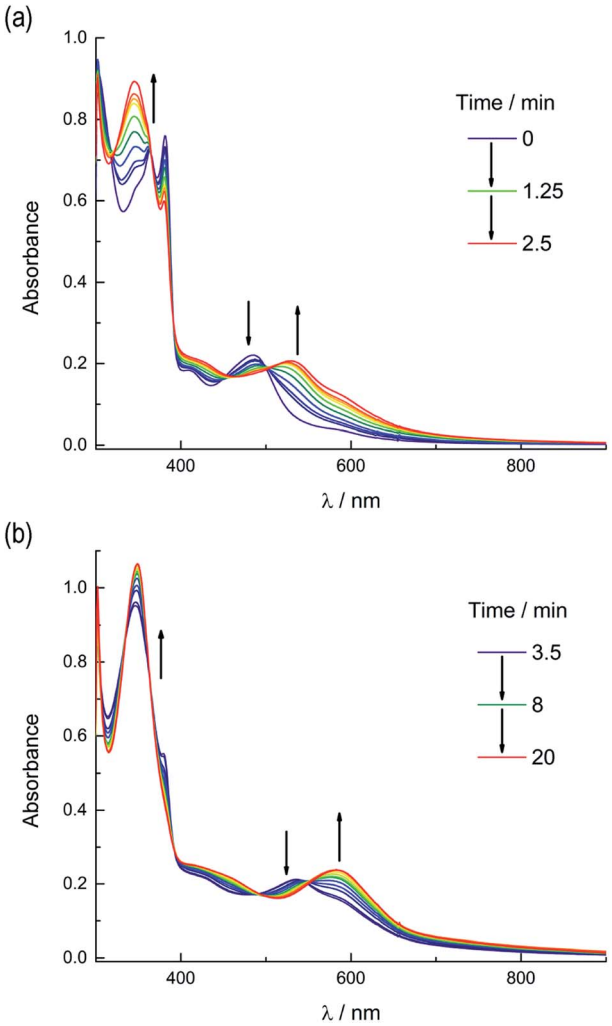

Fig. 6 Changes following irradiation ($\lambda_{irr} \geq 395$ nm) in the electronic absorption spectrum of **2a** in pyridine from (a) $t_{irr} = 0$–2.5 min and (b) $t_{irr} = 3.5$–20 min.

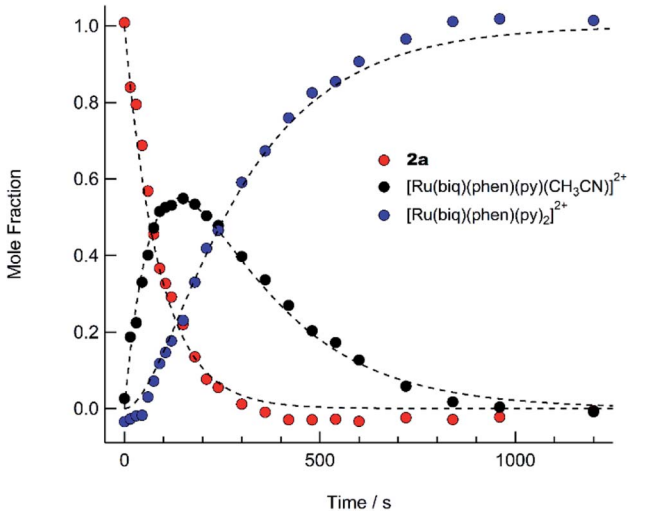

Fig. 7 Time dependent concentrations of **2a** (red circles), *cis*-$[Ru(biq)(phen)(py)(CH_3CN)]^{2+}$ (**I**, black circles), and *cis*-$[Ru(biq)(phen)(py)_2]^{2+}$ following irradiation ($\lambda_{irr} \geq 395$ nm) in pyridine from $t = 0$ to $t = 1200$ s. The dashed lines are least-squares fits to a consecutive reaction model with a system of equations describing the time-dependent concentration of each compound (see text).

S2, and Fig. S13.† The spectra of **2a** and **3**, along with that of the intermediate, **I**, are shown in Fig. S13,† and the time dependent mole fractions of each species were calculated over the course of the photolysis and are displayed in Fig. 7. Fig. 7 shows that the loss of **2a** occurs rapidly, whereby at 70 s, 50% of the starting material remains and no amount is appreciable beyond 300 s. The formation of the intermediate **I** begins as early as 50 s of irradiation and reaches 99% conversion to the final product, **3**, at ~900 s. A maximum fraction of ~55% of the intermediate **I** is apparent at ~150 s (Fig. 7). From the known proportions of the three species the extinction coefficient for the intermediate was estimated and compared to initial and final product values in Fig. S13.†

The PPh_3 ligand photodissociation from **2a** apparent from the sequential formation of photoproducts in Fig. 6 and 7, as well as in the crystal structure of **I**, shows that irradiation of **2a** does not result in the photodissociation of the CH_3CN ligand, such that there is no evidence of the formation of $[Ru(biq)(phen)(PPh_3)(py)]^{2+}$ following irradiation. Instead CH_3CN substitution must occur from further irradiation of the intermediate, *cis*-$[Ru(biq)(phen)(CH_3CN)(S)]^{2+}$ where S = coordinating solvent molecule. It is also important to note that the growth of the ^{1}H NMR peak corresponding to free CH_3CN at 1.96 ppm for the irradiation of **2a** in CD_3CN shown in Fig. 4c does not begin until $t \sim 4$ min, which is consistent with the dissociation of CH_3CN taking place from the intermediate *cis*-$[Ru(biq)(phen)(CH_3CN)(CD_3CN)]^{2+}$ and not directly from **2a**.

In contrast to the results for **2a**, the $^{31}P\{H\}$ NMR of **1a** did not change as a function of irradiation time (Fig. S14†) in CD_3CN, indicating that the PPh_3 ligand is photostable in this complex and does not photodissociate. Together, these results demonstrate the photoinduced ligand exchange of PPh_3 from **2a** upon irradiation with $\lambda_{irr} \geq 395$ nm, while **1a** undergoes only CH_3CN ligand substitution. Steric strain around the Ru(II) center due to the bulky biq ligand is known to influence the exchange of ligands from Ru(II) complexes following irradiation and likely plays a role in the photoinduced PPh_3 exchange in **2a**.[41,65,66] The observed trends highlight a need to further investigate the geometry around the ruthenium center in phosphine complexes to identify the origin of the unusual dissociation of PPh_3 in **2a**.

Structural comparisons

The generally accepted model for photoinduced ligand exchange in Ru(II) polypyridyl complexes is thermal population of a ^{3}LF (ligand field) state from a lower energy ^{3}MLCT (metal-to-ligand charge transfer) state, which places electron density on Ru-L orbital(s) with σ* anti-bonding character, leading to ligand dissociation.[67–70] Distortion in the pseudo-octahedral geometry around ruthenium metal lowers the energy of the e_g-type σ* set, and consequently of the dissociative ^{3}LF state, leading to a decrease in the activation energy required to thermally populate it from the lowest energy ^{3}MLCT state and

increasing the efficiency of ligand exchange. The introduction of steric bulk *via* ligands containing methyl, phenyl, or quinoline moieties has been shown to sufficiently distort the octahedral geometry, resulting in an increase the quantum yield of ligand exchange.[71–74]

In order to better understand if steric effects account for the differences in the photoreactivity of **1a** and **2a**, their solid-state single-crystal X-ray structures were determined and are shown in Fig. 8, along with relevant bond lengths and angles listed in Table 2 with additional X-ray data available in Tables S3 and S4.† The Ru–N bond lengths from the ruthenium center to the bidentate ligand *trans* to the PPh_3 ligand are 0.05 Å longer on average in **2a** (biq) as compared to **1a** (phen), respectively, indicating greater steric strain in the former. The greater steric hindrance in **2a** relative to **1a** is further supported by the Ru1–P1 bond length, which is 0.024 Å longer in **2a**, consistent with a weaker Ru–P bonding interaction in the biquinoline complex. The crystal structure of **2b** (Fig. 8), obtained by irradiating a solution of **2a** in CH_3CN with visible light overnight, possesses Ru–N3 and Ru–N4 bond lengths that are 0.075 and 0.028 Å shorter than in **2a**, respectively, where N3 and N4 are the nitrogen atoms in the biquinoline ligand. Such a decrease in Ru–N bond lengths demonstrates that the photodissociation of PPh_3 relieves steric strain.

Evidence for distortion of the bidentate ligand *trans* to PPh_3 is apparent in the torsion angle, the angle between the two N–C–C planes formed by N3 of the bidentate ligand and the two carbon atoms bridging it to N4, expected to be 0° in an ideal octahedral geometry. In the case of **1a**, the N3–C–C–N4 torsion angle in the phenanthroline ligand is 2(1)°. In contrast, a torsion angle of 10.5(2)° is measured in the biquinoline ligand in **2a**. Further, geometric planes defined by N1–Ru1–N2 and N3–Ru1–N4 would be at 90° angles in an ideal octahedral geometry and deviations from this angle reveal additional steric distortion around the metal center.[4] The angle between these two planes in **1a** was determined to be 88.69°, which is reduced to 81.37° in **2a**. Importantly, in **2b** this angle is 86.93° and the N3–C–C–N4 torsion angle in the biquinoline ligand is 3.1(3)°, showing the substitution of PPh_3 for CH_3CN allows the complex to adopt a geometry closer to the ideal octahedral. It should be noted that the Ru–N5 bond to the CH_3CN ligand does not significantly differ in length (0.006 Å) in **1a** and **2a**.

Table 2 Selected crystallographic bond lengths and angles for **1a**, **2a**, and **2b**

	1a	2a	2b
Bond lengths (Å)			
Ru1–N3	2.106(9)	2.148(1)	2.073(2)
Ru1–N4	2.06(1)	2.112(2)	2.084(2)
Ru1–N5	2.030(2)	2.036(2)	2.046(2)
Ru1–P1/N6	2.343(1)	2.3669(5)	2.034(2)
Torsion angles (°)			
N1–C–C–N2	1.1(4)	2.1(2)	0.6(3)
N3–C–C–N4	2(1)	10.5(2)	3.1(3)
Bond angles (°)			
N1–Ru1–N3	87.7(2)	94.09(9)	100.22(7)
N1–Ru1–P1/N6	93.68(8)	85.26(7)	82.24(7)
N2–Ru1–N3	91.2(2)	81.95(9)	87.52(6)
N3–Ru1–N5	82.1(2)	93.13(9)	93.52(7)
N4–Ru1–P1/N6	98.8(4)	103.63(7)	99.31(7)

The bond angles provided in Table 2 demonstrate additional differences in the steric distortion in **1a**, **2a**, and **2b**. For example, the N1–Ru1–N3 and N2–Ru1–N3 angles show the extent of distortion in the phenanthroline ligand in each complex. Substitution of biq for phen in **2a** pushes N1 towards the phosphine ligand while N2 moves away from P1 to accommodate the large PPh_3 unit, such that the N2–Ru1–N3 angle is nearly 10° greater in **1a** than **2a**. These same angles in **2b** demonstrate that the dissociation of PPh_3 relieves the steric strain between the polypyridyl bidentate ligands by allowing the phenanthroline ligand to move away from biq.

The angles N1–Ru1–P1 and N4–Ru1–P1 show the bulkier biquinoline ligand pushes the phosphine away from biq and toward phen in **2a**, to a significantly greater extent than in the analogous phen in **1a**. Similar to the bond angles, the CH_3CN ligand does not display great distortion. The only notable angle

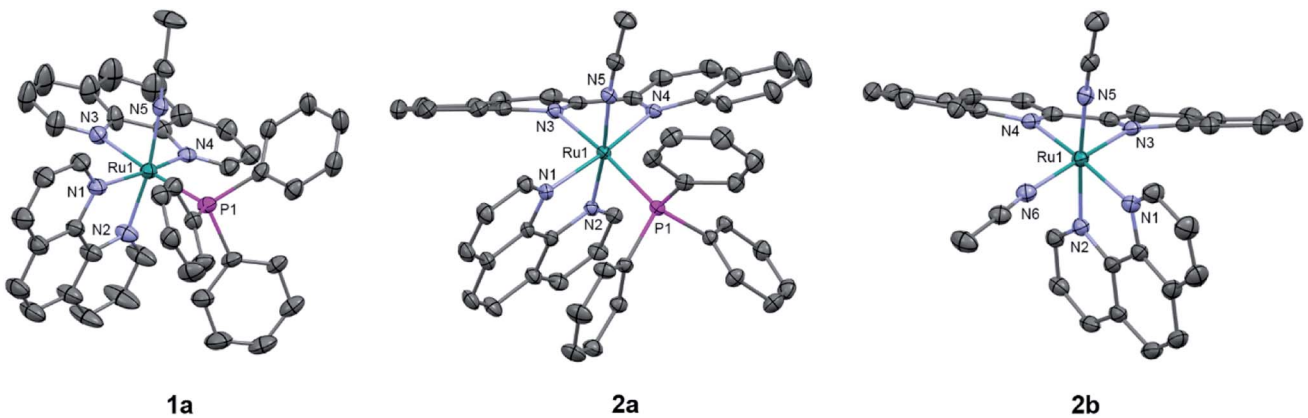

Fig. 8 ORTEP plots of **1a**, **2a**, and **2b** (thermal ellipsoids have been drawn at 50% probability and hydrogen atoms, PF_6^- molecules, and co-crystallized solvent molecules have been omitted for clarity); Ru: cyan, N: light purple, C: grey, and P: magenta.

change is that for N3–Ru1–N5, which is 11° smaller in **1a** than in **2a**, indicating that PPh_3 pushes the acetonitrile ligand towards the *trans* bidentate ligand in **1a** but the presence of the larger biq ligand prevents this displacement in **2a**. In summary, the X-ray crystal structures show that there are significantly greater deviations from octahedral geometry in **2a** as compared to **1a** and **2b**.

Calculations

Density functional theory (DFT) calculations were performed to determine if the bonding and electronic structure in the complexes could further explain the differences in the photoreactivity of **1a** and **2a**. Geometry optimizations in the singlet ground state (^{1}GS) of **1a**, **2a**, and **2b** resulted in structures in good agreement with experimental crystallographic data (Table S4). Table S4† shows that the calculated bond lengths, angles, and torsional angles are in good agreement to those obtained experimentally from the crystal structures of each complex. The ^{1}GS highest occupied molecular orbitals (HOMOs) in **1a** and **2a** exhibit primarily Ru-d orbital character, as is typical for Ru(II) polypyridyl complexes.[63,75–77] The lowest unoccupied molecular orbital (LUMO) in each complex is primarily localized on the ligand *trans* to PPh_3, 1,10-phenanthroline in **1a** and 2,2′-biquinoline in **2a**; the latter agrees with the findings from electrochemistry (Fig. S15, S16 and Table S5†).

Geometry optimizations and vibrational frequency calculations were also performed in the triplet excited states (^{3}ES) of **1a** and **2a**. In the ^{3}ES, longer Ru–$NCCH_3$ and Ru–P bond distances are calculated in both complexes as compared to the corresponding ^{1}GS (Table 3). The calculated Ru–P bonds in the ^{3}ES are similar, 2.475 Å in **1a** and 2.473 Å in **2a**, increasing from 2.411 Å and 2.441 Å in the ^{1}GS, respectively. However, the Ru–$NCCH_3$ bond is 0.04 Å longer in the ^{3}ES of **1a**, 2.055 Å, as compared to that in **2a**, 2.015 Å, which may indicate that the Ru–nitrile bond is weaker in the excited state of **1a** relative to that in **2a**.

The differences in the bonds of **1a** and **2a** in the ^{3}ES were further investigated by calculating the Mayer bond orders (MBOs) of the bonds involving ruthenium (Table 3). MBOs are an extension of Wiberg bond orders and can provide insight into the relative strengths of bonds in transition metal complexes. In the ^{3}ES of **1a**, the MBO of the Ru–$NCCH_3$ bond (Ru1–N5) exhibits a 26.6% decrease as compared to the ^{1}GS and the Ru–N(phen) bond *trans* to CH_3CN (Ru1–N3) displays a dramatic 74.0% increase. These results indicate that the reduced phenanthroline ligand in the excited state exerts a *trans*-type influence on the CH_3CN ligand and weakens the Ru1–N3 bond, likely contributing to its dissociation in the excited state as has been observed in other Ru(II) complexes.[33,78,79] In contrast, the MBO of the bond to CH_3CN only decreases by 11.8% in the triplet state of **2a** and the order of the Ru–N bond *trans* to CH_3CN does not change in the triplet state of **2a**. In addition, the Ru–$NCCH_3$ bond itself is significantly stronger in the ^{3}ES of **2a** as compared to **1a**, 0.576 and 0.441, respectively.

Table 3 Selected Mayer bond orders, MBOs, and calculated bond lengths in the ^{1}GS and lowest ^{3}ES of **1a** and **2a**

	MBOs				Bond Lengths/Å			
	1a		**2a**		**1a**		**2a**	
Bond	^{1}GS	^{3}ES	^{1}GS	^{3}ES	^{1}GS	^{3}ES	^{1}GS	^{3}ES
Ru1–N3[a]	0.370	0.656	0.223	0.223	2.080	2.022	2.096	2.095
Ru1–N5[b]	0.601	0.441	0.653	0.576	2.008	2.055	2.000	2.015
Ru1–N1[c]	0.260	0.408	0.281	0.368	2.136	2.103	2.170	2.146
Ru1–P1	0.760	0.719	0.701	0.659	2.411	2.475	2.441	2.473

[a] Bond to N atom of bidentate ligand *trans* to CH_3CN. [b] Bond to N atom of CH_3CN. [c] Bond to N atom of bidentate ligand *trans* to PPh_3.

Both **1a** and **2a** displayed a ~6% increase in the MBO of the Ru–PPh_3 bond, Ru1–P1 in Table 3, in the ^{3}ES, although the bond is weaker in the excited state of **2a**, MBO = 0.659, than in **1a**, MOB = 0.719. The order of the bond *trans* to the phosphine ligand, Ru1–N1, is calculated to increase by 31.0% in **2a** and 56.9% in **1a**, indicating a *trans*-type influence in both complexes. However, the phenomenon is significantly stronger in **1a** for the bond positioned *trans* to the CH_3CN ligand, Ru1–N3, which may explain why the CH_3CN ligand preferentially photodissociates in this complex.

Mulliken spin density (MSD) calculations were also performed on the lowest energy ^{3}ES of **1a** and **2a**. These calculations determine the unpaired electron density on each atom in the ^{3}ES and can provide information on the nature of the excited state. In complexes with ^{3}LF as the lowest energy triplet excited state, the spin density on the Ru(II) metal center would theoretically equal two. If the lowest energy ^{3}ES is MLCT in nature, the spin density on ruthenium is expected to be one, and any deviation from these whole numbers indicates metal/ligand mixing. The MSD on ruthenium and the summed density on each ligand in the lowest energy ^{3}ES of **1a** and **2a** is shown in Fig. 9. The calculated spin densities on Ru(II) indicate the lowest energy triplet excited state is MLCT in nature with notable ligand character in **1a** and significant mixing from a ligand-centered state in **2a**. The summed spin density on the phenanthroline ligand *trans* to PPh_3 in **1a** is 0.447, lower than the 0.763 sum on the phen ligand *trans* to CH_3CN, further indicating stronger *trans*-type influence on the nitrile ligand in the excited state. In the ^{3}MLCT of **2a** the sum of the spin density on the phen ligand, which is *trans* to CH_3CN, is 0.074 and a sum of 1.433 is calculated on the biquinoline ligand, indicating a significant *trans*-type influence on the PPh_3 ligand. Taken together with the calculated bond lengths and MBOs in the ^{3}MLCT state, it can be concluded that while **1a** exhibits a *trans*-type influence on both monodentate ligands, it is stronger in the case of the CH_3CN ligand which can explain the preferential dissociation of CH_3CN upon irradiation. In the ^{3}MLCT state of **2a** there is no evidence of *trans*-type influence on the nitrile ligand, but a significant degree of *trans*-type influence is calculated for the phosphine ligand. These results, in conjunction with the steric strain evident from the crystal structure, can explain the unexpected photodissociation of the PPh_3 ligand in **2a**.

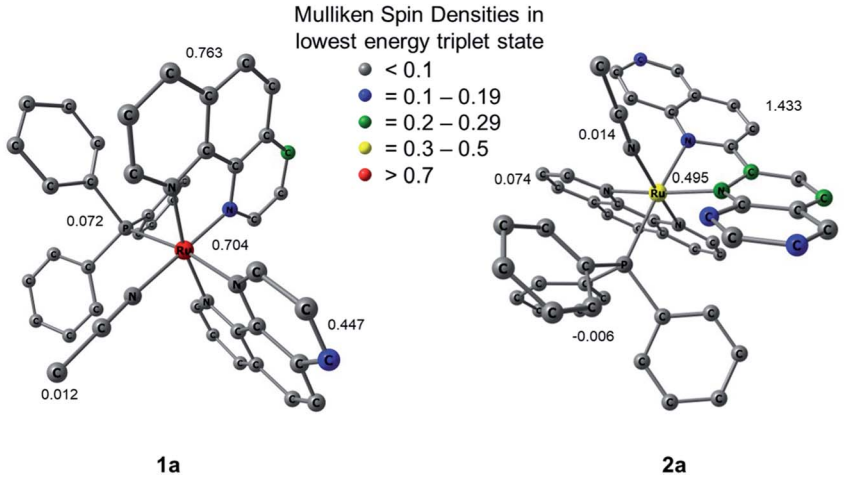

Fig. 9 Mulliken spin densities (MSDs) on ruthenium and the summed densities on each ligand in the calculated lowest energy triplet excited states of **1a** and **2a**.

Cell viability

The effect of photochemical reactivity on the biological behavior of **1a** and **2a** was investigated on the MDA-MB-231 triple-negative breast cancer cell line in the dark and upon irradiation and the results were compared to those of related complexes previously reported.[18,80,81] The half effective concentration, EC_{50}, was determined, which is defined as the concentration of the compound when the viability of the experimental cells is 50% compared to those in the absence of active compound. Complexes **1a** and **2a** were incubated with MDA-MB-231 cells for 1 h and were then either left in the dark or irradiated with blue light for 20 min (λ_{irr} = 460–470 nm, 56 J cm^{-2}). Cellular viability was assessed using the MTT assay after 72 h, where the viability upon treatment with only the vehicle (1% DMSO) only in DMEM (Dulbecco's Modified Eagle Medium) was considered as 100%, and the results are listed in Table 3. Both **1a** and **2a** are non-toxic against MDA-MB-231 cells in the dark with EC_{50}^{D} values of 26.6 ± 1.5 μM and >30 μM, respectively; the latter is above the maximum concentration allowed by the solubility in growth media (30 μM). However, irradiation with blue light significantly increased the toxicities of both complexes, resulting in EC_{50}^{L} = 4.6 ± 0.6 μM for **1a** and EC_{50}^{L} = 7.1 ± 0.2 μM for **2a** (Fig. S17 and S18†). These values of the phototherapeutic index, PI, values defined as EC_{50}^{D}/EC_{50}^{L}, were calculated to be 5.8 and >4.2 for **1a** and **2a**, respectively (Table 4). While complex **1a** exchanges CH_3CN for a solvent water molecule, **2a** releases PPh_3 upon irradiation. The finding that PPh_3 by itself is not toxic against MDA-MB-231 cells both in the dark and when irradiated with blue light (t_{irr} = 20 min, λ_{irr} = 460–470 nm, 56 J cm^{-2}) in the concentrations used for complexes **1a** and **2a** (Fig. S19†) led to the conclusion that the corresponding aqua complexes are the major cause of toxicity upon irradiation.

Comparison of the cell toxicity data of *cis*-$[Ru(bpy)_2(PPh_3)(CH_3CN)]^{2+}$ and *cis*-$[Ru(bpy)_2(CH_3CN)_2]^{2+}$ in Table 3 indicates that the substitution of a CH_3CN ligand for PPh_3 increases the PI value of the ruthenium complex. Complexes **1a** and **2a** exhibit PI values similar to or exceeding that of *cis*-$[Ru(bpy)_2(PPh_3)(CH_3CN)]^{2+}$. These results indicate that the phosphine ligand may positively influence the activity against cancer cells of these ruthenium complexes, a conclusion supported by previous examples of phosphines improving cellular uptake and localizing complexes to the mitochondria, increasing selectivity for cancerous cells over healthy cells,[22] and increasing cytotoxic activity against breast and colon cancer cells of phosphine containing *cis*-configured Pt(II) complexes over that of cisplatin.[21,84–86]

Table 4 EC_{50} values upon irradiation and in the dark and photochemotherapeutic index, PI, for **1a**, **2a**, and related compounds in MDA-MB-231 cancer cells

Complex	EC_{50}^{D}/μM [a]	EC_{50}^{L}/μM [a]	PI [b]
1a	26.6 ± 1.5	4.6 ± 0.6	5.8
2a	>30	7.1 ± 0.2	>4.2
$[Ru(bpy)_2(PPh_3)(CH_3CN)]^{2+}$ [c]	>30	7.0 ± 1.4	>4.3
cis-$[Ru(bpy)_2(CH_3CN)_2]^{2+}$ [d]	244 ± 23	223 ± 94	1.1 ± 0.4

[a] Data are an average of three independent experiments. [b] PI = EC_{50}^{D}/EC_{50}^{L}. [c] From ref. 82; bpy = 2,2′-bipyridine. [d] From ref. 83; IC_{50} values against HeLa cells.

Conclusion

Two new triphenylphosphine-containing complexes, **1a** and **2a**, were synthesized and their ground state spectroscopic and electrochemical properties were characterized, along with their photoinduced ligand exchange and cytotoxicity against a triple-negative breast cancer cell line. Changes in the electronic absorption and NMR spectra of complex **1a** revealed the substitution of a CH_3CN ligand for a solvent molecule following visible light irradiation and a substitutionally inert PPh_3. In contrast, the photolysis of complex **2a** results in the initial exchange of the PPh_3 ligand generating a solvated intermediate, and the latter goes on to absorb a second photon which then undergoes CH_3CN substitution. A comparison of the single crystal X-ray structures reveals that **2a** exhibits greater steric

distortion around the metal center than **1a**, which is subsequently relieved upon the photoinduced exchange of PPh_3 for a less sterically-demanding solvent molecule. To our knowledge, this represents the first report of the photodissociation of a phosphine ligand from a Ru(II) polypyridyl complex. In addition, the ability of phosphine ligands to enhance cellular uptake was shown to enhance the photocytoxicity of **1a** and **2a** against a triple-negative breast cancer cell line relative to related complexes without PPh_3 in their coordination sphere. This work shows that a coordinated PPh_3 ligand can serve as a new architecture for potential therapeutics for use in PCT.

Author contributions

Sean J. Steinke synthesized the complexes and conducted photophysical and photochemical measurements. Eric J. Piechota aided with data analysis and interpretation, Sayak Gupta performed the cell studies, and Curtis E. Moore collected and solved the crystal structures. Jeremy J. Kodanko and Claudia Turro advised their respective group members.

Conflicts of interest

The authors declare no competing financial interest.

Acknowledgements

The authors thank the support from the National Science Foundation (CHE-2102508), as well as Dr J. C. Gallucci for assistance with the collection of the crystal structure data of **2a**.

References

1 N. A. Smith and P. J. Sadler, *Philos. Trans. R. Soc., A*, 2013, **371**, 20120519.
2 (*a*) S. B. Vittardi, R. T. Magar, D. J. Breen and J. J. Rack, *J. Am. Chem. Soc.*, 2021, **143**, 526–537; (*b*) A. W. King, L. Wang and J. J. Rack, *Acc. Chem. Res.*, 2015, **48**, 1115–1122; (*c*) B. A. McClure, N. V. Mockus, D. P. Butcher, Jr, D. A. Lutterman, C. Turro, J. L. Petersen and J. J. Rack, *Inorg. Chem.*, 2009, **48**, 8084–8091.
3 (*a*) J. Karges, S. Kuang, F. Maschietto, O. Blacque, I. Ciofini, H. Chao and G. Gasser, *Nat. Commun.*, 2020, **11**, 1–13; (*b*) M. Jakubaszek, B. Goud, S. Ferrari and G. Gasser, *Chem. Commun.*, 2018, **54**, 13040–13059; (*c*) C. Mari, V. Pierroz, S. Ferrari and G. Gasser, *Chem. Sci.*, 2015, **6**, 2660–2686.
4 (*a*) J. K. White, R. H. Schmehl and C. Turro, *Inorg. Chim. Acta*, 2017, **454**, 7–20; (*b*) J. D. Knoll, B. A. Albani and C. Turro, *Acc. Chem. Res.*, 2015, **48**, 2280–2287; (*c*) J. D. Knoll and C. Turro, *Coord. Chem. Rev.*, 2015, **282–283**, 110–126; (*d*) Y. Sun, M. El Ojaimi, R. Hammit, R. P. Thummel and C. Turro, *J. Phys. Chem. B*, 2010, **114**, 14664–14670.
5 S. Monro, K. L. Colon, H. Yin, J. Roque, P. Konda, S. Gujar, R. P. Thummel, L. Lilge, C. G. Cameron and S. A. McFarland, *Chem. Rev.*, 2019, **119**, 797–828.
6 L. Hammarström, *Acc. Chem. Res.*, 2015, **48**, 840–850.
7 M. R. Gill and J. A. Thomas, *Chem. Soc. Rev.*, 2012, **41**, 3179–3192.
8 L. Marcelis, J. Ghesquiere, K. Garnir, A. Kirsch-De Mesmaeker and C. Moucheron, *Coord. Chem. Rev.*, 2012, **256**, 1569–1582.
9 R. Oun, Y. E. Moussa and N. J. Wheate, *Dalton Trans.*, 2018, **47**, 6645–6653.
10 R. Liu, L. Zhang, J. Zhao, Z. Luo, Y. Huang and S. Zhao, *Adv. Thermoelectr.*, 2018, **1**, 1800041.
11 J. Dang, H. He, D. Chen, L. Yin and L. Biomater, *Sci*, 2017, **5**, 1500–1511.
12 Y. Mir, J. E. van Lier, B. Paquette and D. Houde, *Photochem. Photobiol.*, 2008, **84**, 1182–1186.
13 D. Havrylyuk, D. K. Heidary, Y. Sun, S. Parkin and E. C. Glazer, *ACS Omega*, 2020, **5**, 18894–18906.
14 H. Shi, C. Imberti and P. J. Sadler, *Inorg. Chem. Front.*, 2019, **6**, 1623–1638.
15 V. H. S. van Rixel, V. Ramu, A. B. Auyeung, N. Beztsinna, D. Y. Leger, L. N. Lameijer, S. T. Hilt, S. E. Le Devedec, T. Yildiz, T. Betancourt, M. B. Gildner, T. W. Hudnall, V. Sol, B. Liagre, A. Kornienko and S. Bonnet, *J. Am. Chem. Soc.*, 2019, **141**, 18444–18454.
16 M. K. Herroon, R. Sharma, E. Rajagurubandara, C. Turro, J. J. Kodanko and I. Podgorski, *Biol. Chem.*, 2016, **397**, 571–582.
17 M. Huisman, J. K. White, V. G. Lewalski, I. Podgorski, C. Turro and J. J. Kodanko, *Chem. Commun.*, 2016, **52**, 12590–12593.
18 K. Arora, M. Herroon, M. H. Al-Afyouni, N. P. Toupin, T. N. Rohrabaugh, L. M. Loftus, I. Podgorski, C. Turro and J. J. Kodanko, *J. Am. Chem. Soc.*, 2018, **140**, 14367–14380.
19 T. N. Rohrabaugh, A. M. Rohrabaugh, J. J. Kodanko, J. K. White and C. Turro, *Chem. Commun.*, 2018, **54**, 5193–5196.
20 A. Li, R. Yadav, J. K. White, M. K. Herroon, B. P. Callahan, I. Podgorski, C. Turro, E. E. Scott and J. J. Kodanko, *Chem. Commun.*, 2017, **53**, 3673–3676.
21 (*a*) A. A. Khan, K. S. Allemailen, A. Almatroudi, S. A. Almatroodi, M. A. Alsahli and A. H. Rahmani, *J. Drug Delivery Sci. Technol.*, 2021, **61**, 102315; (*b*) B. Rousselle, F. Bouyer, J. Bayardon, M. Laly, F. Ghiringhelli, Y. Rousselin, E. Bodio and R. Malacea-Kabbara, *Dalton Trans.*, 2021, **50**, 4880–4889; (*c*) M. Ali, L. Dondaine, A. Adolle, C. Sampaio, F. Chotard, P. Richard, F. Denat, A. Bettaieb, P. Le Gendre, V. Laurens, C. Goze, C. Paul and E. Bodio, *J. Med. Chem.*, 2015, **58**, 4521–4528.
22 R. S. Correa, L. M. Bomfim, K. M. Oliveira, D. R. M. Moreira, M. B. P. Soares, J. Ellena, D. P. Bezerra and A. A. Batista, *J. Biol. Inorg Chem.*, 2019, **198**, 110751.
23 Y. R. Pérez and R. Etchenique, *Photochem. Photobiol. Sci.*, 2019, **18**, 208–212.
24 S. M. Veronica, M. Alvarez, O. Filevich, R. Etchenique and A. del Campo, *Langmuir*, 2012, **28**, 1217–1221.
25 L. Zayat, M. G. Noval, J. Campi, C. I. Calero, D. J. Calvo and R. Etchenique, *Chembiochem*, 2007, **8**, 2035–2038.
26 S. K. Lee, M. Kondo, G. Nakamura, M. Okamura and S. Masaoka, *Chem. Commun.*, 2018, **54**, 6915–6918.

27 I. M. Dixon, E. Lebon, G. Loustau, P. Sutra, L. Vendier and A. Juris, *Dalton Trans.*, 2008, 5627–5635.
28 E. Lebon, I. M. Dixon, L. Vendier, A. Igau and P. Sutra, *Inorg. Chim. Acta*, 2007, **360**, 1235–1239.
29 I. M. Dixon, E. Lebon, P. Sutra and A. Igau, *Chem. Soc. Rev.*, 2009, **38**, 1621–1634.
30 D. V. Pinnick and B. Durham, *Inorg. Chem.*, 1984, **23**, 1440–1445.
31 L. Zayat, O. Filevich, L. Baraldo and R. Etchenique, *Philos. Trans. R. Soc., A*, 2013, **371**, 20120330.
32 J. D. Knoll, B. A. Albani and C. Turro, *Chem. Commun.*, 2015, **51**, 8777–8780.
33 L. M. Loftus, A. Li, K. L. Fillman, P. D. Martin, J. J. Kodanko and C. Turro, *J. Am. Chem. Soc.*, 2017, **139**, 18295–18306.
34 T. N. Rohrabaugh, Jr., K. A. Collins, C. Xue, J. K. White, J. J. Kodanko and C. Turro, *Dalton Trans.*, 2018, **47**, 11851–11858.
35 W.-S. Huang, S. Liu, D. Zou, M. Thomas, Y. Wang, T. Zhou, J. Romero, A. Kohlmann, F. Li, J. Qi, L. Cai, T. A. Dwight, Y. Xu, R. Xu, R. Dodd, A. Toms, L. Parillon, X. Lu, R. Anjum, S. Zhang, F. Wang, J. Keats, S. D. Wardwell, Y. Ning, Q. Xu, L. E. Moran, Q. K. Mohemmad, H. G. Jang, T. Clackson, N. I. Narasimhan, V. M. Rivera, X. Zhu, D. Dalgarno and W. C. Shakespeare, *J. Med. Chem.*, 2016, **59**, 4938–4964.
36 R. Wang, Y. Chen, X. Zhao, S. Yu, B. Yang, T. Wu, J. Guo, C. Hao, D. Zhao and M. Cheng, *Eur. J. Med. Chem.*, 2019, **183**, 111716.
37 J. Tu, L. T. Song, H. L. Zhai, J. Wang and X. Y. Zhang, *Int. J. Biol. Macromol.*, 2018, **118**, 1149–1156.
38 S. Bischoff and M. Kant, *Catal. Today*, 2001, **66**, 183–189.
39 A. Riisager, K. M. Eriksen, P. Wasserscheid and R. Fehrmann, *Catal. Lett.*, 2003, **90**, 149–153.
40 B. A. Harper, D. A. Knight, C. George, S. L. Brandow, W. J. Dressick and C. S. Dalcey, *Inorg. Chem.*, 2003, **42**, 516–524.
41 B. A. Albani, C. B. Durr and C. Turro, *J. Phys. Chem. A*, 2013, **117**, 13885–13892.
42 Z. Assefa and D. M. Stanbury, *J. Am. Chem. Soc.*, 1997, **119**, 521–530.
43 M. A. Bennett and A. K. Smith, *J. Chem. Soc., Dalton Trans.*, 1974, 233–241.
44 A. Alberti, P. Astolfi, P. Carloni, L. Greci, C. Rizzoli and P. Stipa, *New J. Chem.*, 2015, **39**, 8964–8970.
45 V. V. Pavlishchuk and A. W. Addison, *Inorg. Chim. Acta*, 2000, **298**, 97–102.
46 M. J. Frisch, G. W. Trucks, H. B. Schlegel, G. E. Scuseria, M. A. Robb, J. R. Cheeseman, G. Scalmani, V. Barone, G. A. Petersson, H. Nakatsuji, X. Li, M. Caricato, A. Marenich, J. Bloino, B. G. Janesko, R. Gomperts, B. Mennucci, H. P. Hratchian, J. V. Ortiz, A. F. Izmaylov, J. L. Sonnenberg, D. Williams-Young, F. Ding, F. Lipparini, F. Egidi, J. Goings, B. Peng, A. Petrone, T. Henderson, D. Ranasinghe, V. G. Zakrzewski, J. Gao, N. Rega, G. Zheng, W. Liang, M. Hada, M. Ehara, K. Toyota, R. Fukuda, J. Hasegawa, M. Ishida, T. Nakajima, Y. Honda, O. Kitao, H. Nakai, T. Vreven, K. Throssell, J. A. Montgomery Jr, J. E. Peralta, F. Ogliaro, M. Bearpark, J. J. Heyd, E. Brothers, K. N. Kudin, V. N. Staroverov, T. Keith, R. Kobayahsi, J. Normand, K. Raghavachari, A. Rendell, J. C. Burant, S. S. Iyengar, J. Tomasi, M. Cossi, J. M. Millam, M. Klene, C. Adamo, R. Cammi, J. W. Ochterski, R. L. Martin, K. Morokuma, O. Farkas, J. B. Foresman and D. J. Fox, *Gaussian 09, revision E.01*. Gaussian, Inc.: Wallingford, CT, 2016.
47 D. Andrae, U. Häußermann, M. Dolg, H. Stoll and H. Preuß, *Theor. Chim. Acta*, 1990, **77**, 123–141.
48 A. Schäfer, H. Horn and R. Ahlrichs, *J. Chem. Phys.*, 1992, **97**, 2571–2577.
49 J. P. Perdew, K. Burke and M. Ernzerhof, *Phys. Rev. Lett.*, 1996, **77**, 1396.
50 J. P. Perdew, K. Burke and M. Ernzerhof, *Phys. Rev. Lett.*, 1996, **77**, 3865–3868.
51 A. D. Becke, *Phys. Rev. A*, 1988, **38**, 3098–3100.
52 C. Lee, W. Yang and R. G. Parr, *Phys. Rev. B: Condens. Matter Mater. Phys.*, 1988, **37**, 785–789.
53 B. Miehlich, A. Savin, H. Stoll and H. Preuss, *Chem. Phys. Lett.*, 1989, **157**, 200–206.
54 Chemcraft; *Graphical Software for Visualization of Quantum Chemistry Computations*. https://www.chemcraftprog.com.
55 S. I. Gorelsky and A. B. P. Lever, *J. Organomet. Chem.*, 2001, **635**, 187–196.
56 S. I. Gorelsky, *AOMix: Program for Molecular Orbital Analysis*, 2015.
57 A. G. Orpen and N. G. Connelly, *J. Chem. Soc., Chem. Commun.*, 1985, **19**, 1310–1311.
58 D. M. Klassen, *Chem. Phys. Lett.*, 1982, **93**, 383–386.
59 M. Mitoraj and A. Michalak, *Organometallics*, 2007, **26**, 6576–6580.
60 B. A. Albani, B. Peña, K. R. Dunbar and C. Turro, *Photochem. Photobiol. Sci.*, 2014, **13**, 272–280.
61 P. Bonneson, J. L. Walsh, W. T. Pennington, A. W. Cordes and B. Durham, *Inorg. Chem.*, 1983, **22**, 1761–1765.
62 A. Juris, S. Campagna, V. Balzani, G. Gremaud and A. von Zelewsky, *Inorg. Chem.*, 1988, **27**, 3652–3655.
63 L. M. Loftus, K. F. Al-Afyouni, T. N. Rohrabaugh Jr, J. C. Gallucci, C. E. Moore, J. J. Rack and C. Turro, *J. Phys. Chem. C*, 2019, **123**, 10291–10299.
64 L. M. Loftus, K. F. Al-Afyouni and C. Turro, *Chem. - Eur. J.*, 2018, **24**, 11550–11553.
65 E. Wachter, D. K. Heidary, B. S. Howerton, S. Parkin and E. C. Glazer, *Chem. Commun.*, 2012, **48**, 9649–9651.
66 E. Baranoff, J.-P. Collin, J. Furusho, Y. Furusho, A.-C. Laemmel and J.-P. Sauvage, *Inorg. Chem.*, 2002, **41**, 1215–1222.
67 J. V. Caspar and T. J. Meyer, *Inorg. Chem.*, 1983, **22**, 2444–2453.
68 B. Durham, J. V. Caspar, J. K. Nagle and T. J. Meyer, *J. Am. Chem. Soc.*, 1982, **104**, 4803–4810.
69 B. Durham, J. L. Walsh, C. L. Carter and T. J. Meyer, *Inorg. Chem.*, 1980, **19**, 860–865.
70 G. H. Allen, R. P. White, D. P. Rillema and T. J. Meyer, *J. Am. Chem. Soc.*, 1984, **106**, 2613–2620.

71 J. D. Knoll, B. A. Albani, C. B. Durr and C. Turro, *J. Phys. Chem. A*, 2014, **118**, 10603–10610.
72 S. Bonnet, J. P. Collin, J. P. Sauvage and E. Schofield, *Inorg. Chem.*, 2004, **43**, 8346–8354.
73 A.-C. Laemmel, J.-P. Collin and J.-P. Sauvage, *Eur. J. Inorg. Chem.*, 1999, 383–386.
74 B. S. Howerton, D. K. Heidary and E. C. Glazer, *J. Am. Chem. Soc.*, 2012, **134**, 8324–8327.
75 M. H. Al-Afyouni, T. N. Rohrabaugh, K. F. Al-Afyouni and C. Turro, *Chem. Sci.*, 2018, **9**, 6711–6720.
76 M. Abrahamsson, M. Jäger, R. J. Kumar, T. Österman, P. Persson, H. C. Becker, O. Johansson and L. Hammarström, *J. Am. Chem. Soc.*, 2008, **130**, 15533–15542.
77 J. Romanova, Y. Sadik, M. R. Ranga Prabhath, J. D. Carey and P. D. Jarowski, *J. Phys. Chem. C*, 2017, **121**, 2333–2343.
78 E. Galardon, P. Le Maux, L. Toupet and G. Simonneaux, *Organometallics*, 1998, **17**, 565–569.
79 A. C. H. Da Silva, J. L. F. Da Silva and D. W. Franco, *Dalton Trans.*, 2016, **45**, 4907–4915.
80 S. D. Ramalho, R. Sharma, J. K. White, N. Aggarwal, A. Chalasani, M. Sameni, K. Moin, P. C. Vieira, C. Turro, J. J. Kodanko and B. F. Sloane, *PLoS One*, 2015, **10**, e0142527/1–e0142527/17.
81 N. P. Toupin, S. Nadella, S. J. Steinke, C. Turro and J. J. Kodanko, *Inorg. Chem.*, 2020, **59**, 3919–3933.
82 A. P. Lanquist, S. Gupta, M. Al-Afyouni, J. J. Kodanko and C. Turro, *Chem. Sci.*, 2021, **12**, 12056–12067.
83 B. A. Albani, B. Peña, N. A. Leed, N. A. B. G. de Paula, C. Pavani, M. S. Baptista, K. R. Dunbar and C. Turro, *J. Am. Chem. Soc.*, 2014, **136**, 17095–17101.
84 H. Scheffler, Y. You and I. Ott, *Polyhedron*, 2010, **29**, 66–69.
85 V. Gandin, A. P. Frenandes, M. P. Rigobello, B. Dani, F. Sorrentino, F. Tisato, A. Björnstedt, A. Bindoli, A. Sturaro, R. Rella and C. Marzano, *Biochem. Pharmacol.*, 2010, **79**, 90–101.
86 C. Icsel, V. T. Yilmaz, B. Cevatemre, M. Aygun and E. Ulukaya, *J. Biol. Inorg Chem.*, 2020, **25**, 75–87.